JET–P(99)06

G Huysmans et al

MHD Stability of Optimised Shear Discharges in JET

JET–P(99)06

MHD Stability of Optimised Shear Discharges in JET

G T A Huysmans, T C Hender[1], B Alper, Y Baranov,
D N Borba[2], G D Conway, G Cottrell, C Gormezano,
P Helander[1], O J Kwon[4], M F F Nave[2], A C C Sips,
F X Söldner, E J Strait[3], W Zwingmann, The JET Team.

JET Joint Undertaking, Abingdon, Oxfordshire, OX14 3EA,
[1]EURATOM/UKAEA Fusion Association, Culham Science Centre, Abingdon, OX14 3DB, UK.
[2]Associação EURATOM/IST, Lisbon, Portugal.
[3]General Atomics, San Diego, CA92186-5608, USA.
[4]Taegu University, Taegu, Republic of Korea.

Preprint of a Paper submitted for publication in Nuclear Fusion

March 1999

ABSTRACT

The main limitation to the performance of the JET optimised shear discharges is due to MHD instabilities mostly in the form of a disruptive limit. The structure of the MHD mode observed as a precursor to the disruption as measured from soft x-ray and ECE diagnostics shows a global ideal MHD mode. The measured mode structure is in good agreement with the calculated mode structure of the pressure driven kink mode. The disruptions occur at relatively low normalised beta ($1< \beta_N < 2$) in good agreement with calculated ideal MHD stability limits for the n=1 pressure driven kink mode. These low limits are mainly due to the extreme peaking factor of the pressure profiles. Other MHD instabilities observed in the JET optimised shear discharges include, usually benign, chirping modes. These modes, which occur in bursts during which the frequency changes, have the same mode structure as the disruption precursor but are driven unstable by fast particles.

1. INTRODUCTION

The good performance of the JET Optimised Shear (OS) discharges [1] is due to a characteristic transport barrier at about mid-radius in the plasma. The occurrence of the transport barrier is related to the shape of the q-profile. A typical q-profile in the JET optimised shear discharges has a low shear in the plasma centre with a value of q on axis between 1.5 and 2. These q-profiles are obtained by neutral beam and RF heating of the plasma during the ramp up phase of the plasma current. The ramp rate is typically 400kA/s. Low power lower-hybrid and RF heating are applied before the main heating to slow down the current diffusion. With the start of the beam heating, an internal transport barrier forms resulting in extremely high central ion temperatures and a peaked pressure profile. The continued ramp of the plasma current and the reduced heat flow to the plasma edge keeps the discharge in L-mode. The highest neutron rate is usually in the L-mode phase. When the plasma eventually goes into an H-mode the internal barrier slowly degrades and the good performance is terminated by a giant ELM. Discharges with an internal transport barrier combined with an ELMy H-mode edge transport barrier have also been produced in JET [2]. Such a combination of edge and internal transport barriers offer good prospects for achieving steady state plasmas.

The combination of a q-profile with low central shear and a minimum q well above one, i.e. no q=1 surface, and a peaked pressure profile gives rise to MHD instabilities which are quite different from the instabilities observed in the Hot-Ion H-mode, the conventional high performance regime in JET [3]. Obviously, sawteeth, one of the main performance limiting MHD instabilities in Hot-Ion H-modes, require a q=1 surface to become unstable and are therefore absent in OS discharges. Also, the best performance in the OS regime is usually obtained when the plasma has an L-mode edge, i.e. without the large edge pressure gradients in the edge pedestal. This avoids the Outer Modes and giant ELMs common in Hot-Ion H-modes which are driven by the edge pressure gradient and the associated bootstrap current [4]. Only when the central pres-

sure gradients of the OS plasma are combined with an ELM free H-mode edge are giant ELMs found in OS discharges.

Although the MHD instabilities which are limiting the performance in the Hot-Ion H-mode discharges can be avoided in the OS regime, this does not mean that a higher value of normalised beta can easily be obtained. In the OS regime different MHD instabilities occur which are related to the steep central pressure gradients and the particular shape of the q-profile. The most common limitation to the performance in the JET OS discharges is due to disruptions. Chirping modes, i.e modes with a fast changing frequency, are also regularly observed but these modes are in general benign. Also very commonly observed are Alfven eigenmodes (AE). They are driven by the fast particles from the ICRH heating. The AE are more unstable in the OS discharges, as compared to the Hot-Ion H-mode regime, due to the higher values for the central q. The stability of Toroidal Alfven Eigenmodes (TAE) in the OS regime is discussed in detail in [5]. Other MHD modes observed include m/n=2/1 tearing modes which form islands at the q=2 surface. The tearing modes are relatively rare and prevent the formation of the transport barrier [6].

This paper focuses on the most commonly observed low frequency (<100 kHz) MHD modes in the JET Optimised Shear discharges. In the next section, the disruptions and their precursors are analysed. The MHD instability is identified by comparing the measured mode structure from both the ECE and SXR diagnostics with the calculated mode structures. The MHD stability limits of the relevant instabilities and their dependence on the q-profile and the peaking of the pressure profile are presented. The chirping modes are discussed in the third section. Other, less frequently observed MHD instabilities are discussed in the fourth section.

2. DISRUPTIONS

The major limitation to the maximum performance of Optimised Shear discharges is due to the occurrence of disruptions. The normalised beta β_N (= $<\beta>$ a[m] B [T]/ I [MA], where $<\beta>$ is the toroidal beta, a the minor radius, B the vacuum toroidal magnetic field and I the total plasma current), at which the disruptions are triggered, can be relatively low. Figure 1 shows the values of β_N at the time just before the disruption as a function of the total additional heating power for all disruptions in the Optimised Shear experimental campaign with the Mark-IIA divertor. This includes disruptions at low beta (low heating power) which are most likely

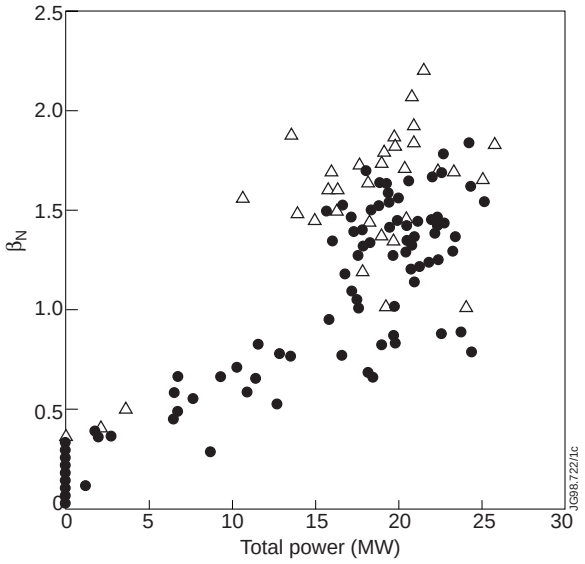

Fig.1. The normalised beta β_N at the time of a disruption (circles) in JET optimised shear discharges. Included is a selection of discharges without disruptions (triangles).

due to the fast current ramp rate. The highest β_N at the time of a disruption is 1.8. Disruptions can occur at much lower values of $\beta_N \sim 0.5$. The highest β_N in an Optimised Shear plasma that does not disrupt is 2.2. However, achieving a high normalised beta has, so far, not been an explicit goal in the JET Optimised Shear experiments. The shape of the q-profiles has been dictated by the requirement of the creation of a transport barrier at the available heating. (The threshold power appears to be lower when there is a q=2 surface with a small volume inside the q=2 surface.) The disruptions can be avoided by controlling the total heating power during the discharges such that the plasma stays below the MHD stability limit (see section 2.3).

2.1 The disruption precursor

In some cases the disruption is preceded by a clear precursor which can be observed in the magnetics, the fast ECE, SXR and reflectometer data. Figure 2b shows an example (discharge #40572) of a disruption precursor in the data of one pick-up coil. The time traces of this discharge are shown in Fig. 2a. The toroidal mode number as determined from a toroidal array of pick-up coils is n=1. The initial frequency of the mode is close to the central rotation frequency of the plasma which is 30 kHz. The mode amplitude grows exponentially with a characteristic time of 0.2ms. As the mode grows the frequency slows down until it locks to the wall, at which point the plasma disrupts. In this example, the time from the start of the mode up to the disruption is about 2ms, in other cases where the growth rate of the precursor is smaller it can take up to 6 ms.

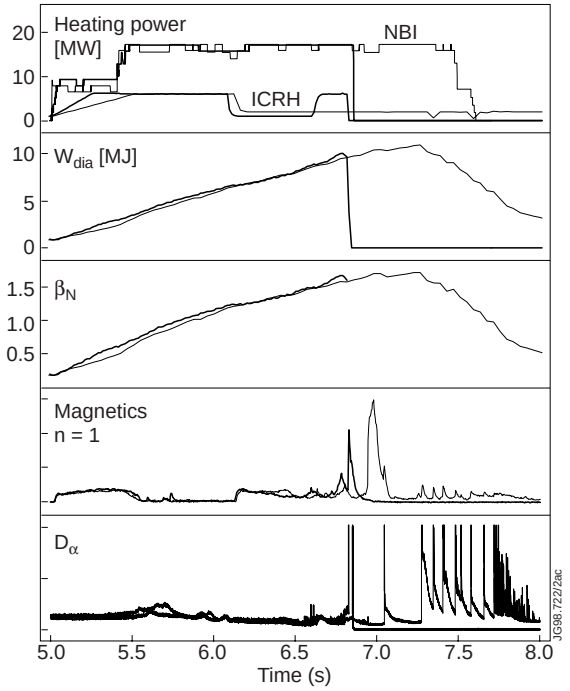

Fig.2a The evolution of the heating power, the stored energy, normalised beta, the n=1 magnetics data and the D_α signal as a function of time for discharge #40572. Included are the traces (thin lines) for a similar discharge #40552 which does not disrupt.

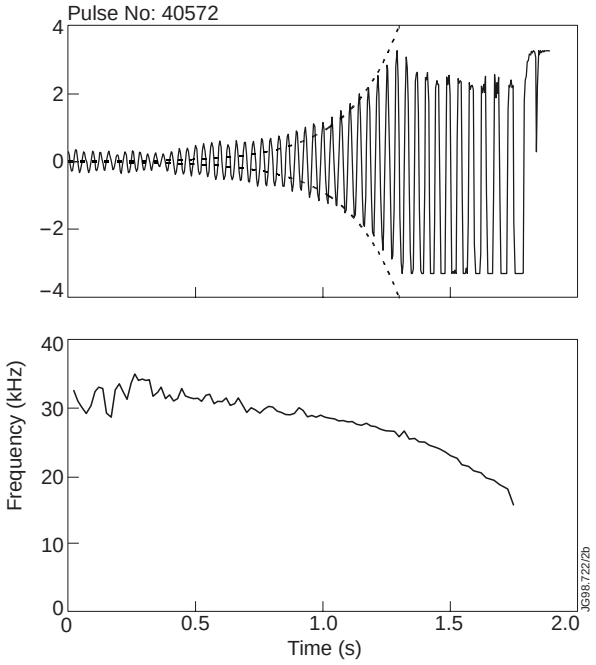

Fig.2b The disruption precursor in discharge #40572 as seen in magnetic pick-up coil data. The top trace is the data from one pick-up coil (dB_θ/dt). The bottom trace is the frequency of the mode as a function of time. The signal saturates the detector after 1.3 ms.

The radial structure of the disruption precursor can be obtained from the 48 channel heterodyne ECE radiometer [7] with a sample rate of 250 kHz. In calculating the radial position of ECE channels, it is essential to use the total magnetic field from an equilibrium which includes the experimental pressure profile with the large gradients at the transport barrier. The diamagnetic effect due to the pressure gradients reduces the toroidal field significantly. Not taking this effect into account leads to an over estimate of the gradients in the electron temperature in the transport barrier. Figure 3 shows the time evolution of the electron temperature profile just before the disruption from 14 channels between R=3.1 and 3.75 m. Assuming that the electron temperature profile moves with the flux surfaces, the displacement of the flux surfaces due to the MHD instability causing the disruption can be determined. In the last oscillation before the disruption the maximum displacement grows to a large amplitude of ±15 cm. The perturbation becomes strongly non-sinusoidal at these large amplitudes. This is due to the growth of an n=2 mode with double the frequency of the n=1 mode. The phase of the n=2 mode is such that the n=2 adds to the n=1 at the maxima (in radius) of the n=1, i.e. where the n=1 displacement increases the pressure gradient in the low field side mid-plane. At the minima of the n=1, the n=2 reduces the amplitude of the total perturbation. This n=2 mode is probably a secondary instability driven unstable by the increased pressure gradients due to the n=1 mode. Figure 4 shows the displacement of the n=1 component of the disruption precursor from 3 different time windows as a function of the major radius. The amplitudes are obtained by fitting to the contours of T_e of Fig. 3 with : $R(t_i) = R_{av} + A_{n=1} \cos(\omega t_i) e^{t/\tau}$ where R_{av} , $A_{n=1}$, are the fitting parameters representing the average radius of the contour, and the amplitude of the n=1 component of the displacement. The

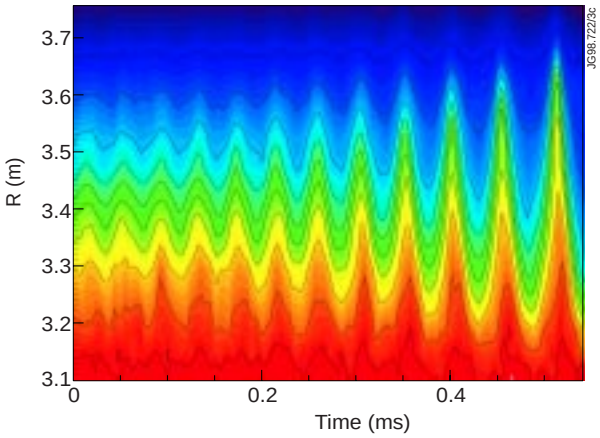

Fig.3 Contours of the time evolution of the electron temperature profile at the time of the disruption precursor. Each contour (black lines) are 1 keV apart. The maximum temperature is 12.6 keV on axis at R = 3.1 m. The plasma boundary is at R = 3.9 m.

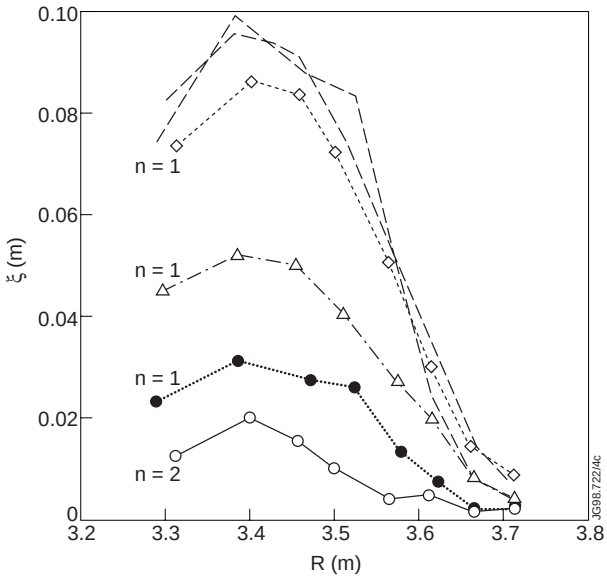

Fig.4 The displacement of the flux surfaces as a function of the major radius due to the disruption precursor for 3 time intervals (0.17-0.26 ms, 0.26-0.38 ms and 0.34-0.45ms) . The curves with closed symbols are the n=1 component. The open circles are the n=2 component for the last time interval (corresponding to the closed diamonds for the n=1). The dashed curves are the first two displacements from the first two intervals scaled with a growth time of 0.18 ms.

growth time is τ = 0.18 ms. In the last period before the disruption the n=2 component can also be determined and is included in the fit. The viewing line of the ECE diagnostic is 13 cm below the magnetic axis. This means that the displacement determined from the ECE very close to the axis does not correspond to the perpendicular displacement in the outboard mid-plane. However this affects only the radii close to the magnetic axis where, in any case, the displacement cannot be determined due to the temperature gradients going to zero on axis. The shape of the n=1 mode does not change as the amplitude increases exponentially (as shown in Fig.4). The n=1 displacement has an off-axis maximum close to the q=2 surface at R=3.4m. There are no phase changes across the radius indicating that the mode is an ideal MHD mode.

More information on the mode structure of the disruption precursor can be obtained from the SXR data. The JET SXR diagnostic [8] consists of 6 cameras with about 180 viewing lines in one poloidal plane. This large number of viewing lines allows an accurate tomographic reconstruction of the mode structure. An advantage of the tomographic reconstruction of the SXR data is that it can yield the radial structure of the different poloidal harmonics of the perturbations, i.e the full mode structure in the poloidal plane. This can be used for a detailed comparison of the observed mode structures with the results from MHD stability calculations. The method used for the tomographic reconstruction is described in more detail in appendix A.

The evolution of the SXR emission profile during the disruption is analysed by reconstructing the profile in the last but one full period before the disruption. Assuming a rigid rotation of the mode structure, i.e. the mode has one single frequency, consecutive time points can be interpreted as measurements at different toroidal angles. Since the mode is growing exponentially, the data at different times has to be scaled with the growth rate, τ = 0.18ms. In the tomographic inversion the data from 8 time slices (with a total of 1024 data points) from one period of the precursor oscillation is used. The mode numbers used are m/n=0/0, 1/1, 2/1, 2/2, 3/2 and 4/2 as basis functions. The radial dependence of each m/n combination is represented by 8 cubic B-splines. The resulting shape of the SXR emission profile in the poloidal plane is shown in Fig. 5 for 8 time slices which are 8μs apart.

From reconstructions using both sine and cosine components it is clear that the sine components are small. An equally good fit is obtained with just cosine components, so in the result shown only the cosine components have been used.

The dominant movement of the central part of the plasma due to the mode is a combination of a rotation of the magnetic axis and an oscillation in the elongation of the flux surfaces. The rotation is due to a m/n=1/1 component, the elongation changes are due to a m/n=2/1 component. The m/n=1/1 and m/n=2/1 add on the low field side and are of opposite sign on the high field side. The radial dependence of the harmonics is shown in Fig. 6 for both the n=1 and n=2 harmonics (as a function of $\sqrt{\psi}$ where ψ is the normalised poloidal flux). All poloidal harmonics (except the m=0 harmonic) have to go to zero on axis to avoid a discontinuity in the perturbation on axis (regularity condition). Also shown is the perturbation of the SXR emission profile as a

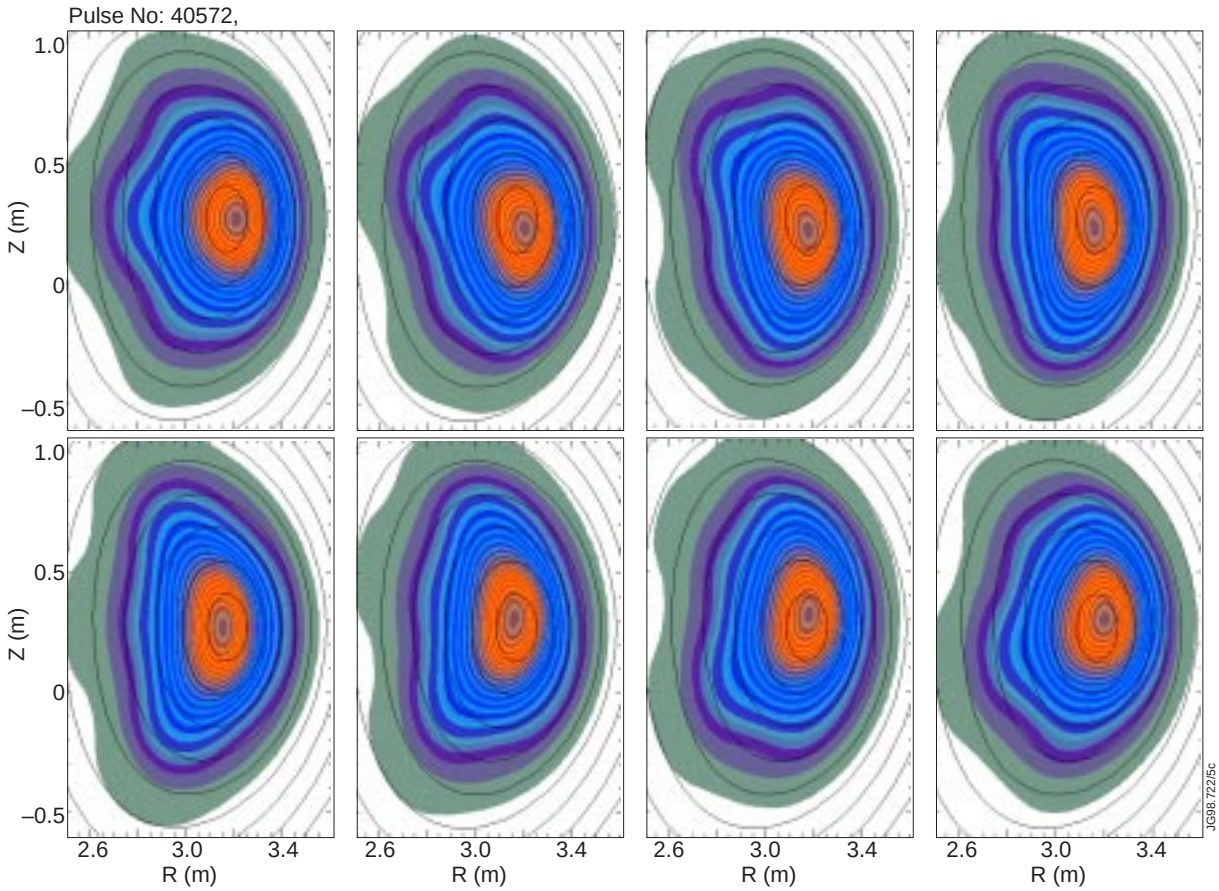

Fig.5 The evolution of the SXR emission profile from t=0.41 ms to 0.47ms (see Fig 3). The time difference between each frame is 8 μs. Shown are contours of constant SXR emission in the region 2.5 m < R <3.7 m, -0.7 m < Z < 1.2 m. The black contours are the equilibrium flux surfaces which are used as the co-ordinate system in the reconstruction.

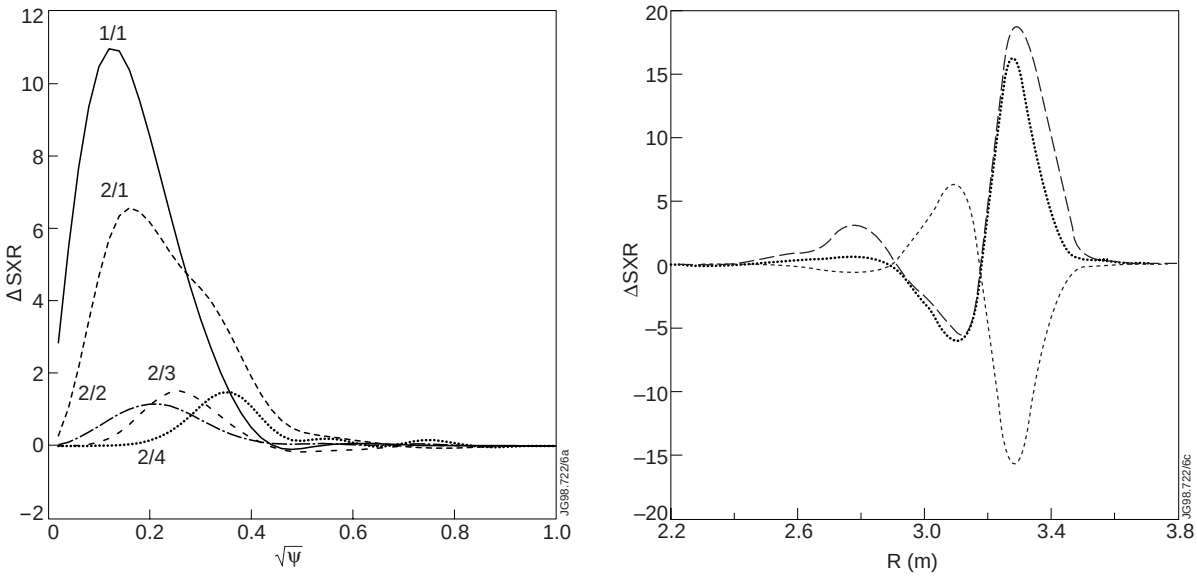

Fig.6a On the left, the poloidal harmonics of the n=1 and of the n=2 components of the perturbation of the SXR emission for the same period as in figure 5. On the right, the total perturbation of the SXR emission profile at two toroidal angles, $\phi=0$ (thick line) and π (thin line). The dashed curve is the negative of the $\phi=\pi$ curve.

function of the radius in the mid-plane for two values of the toroidal angle. The difference between the perturbation at $\phi=0$ and the negative of the perturbation at $\phi=\pi$ is due to the n=2 component. The n=2 adds to the n=1 mode when the n=1 perturbation is positive on the low field (outboard) side. Thus both the poloidal and toroidal components of the perturbation in the SXR emission are in phase so that they add to the maximum amplitude on the outboard mid-plane. This is the region of bad curvature where the plasma pressure is destabilising. Fig. 6b shows the n=1, the n=2 and the total perturbation in the SXR emission at one toroidal angle.

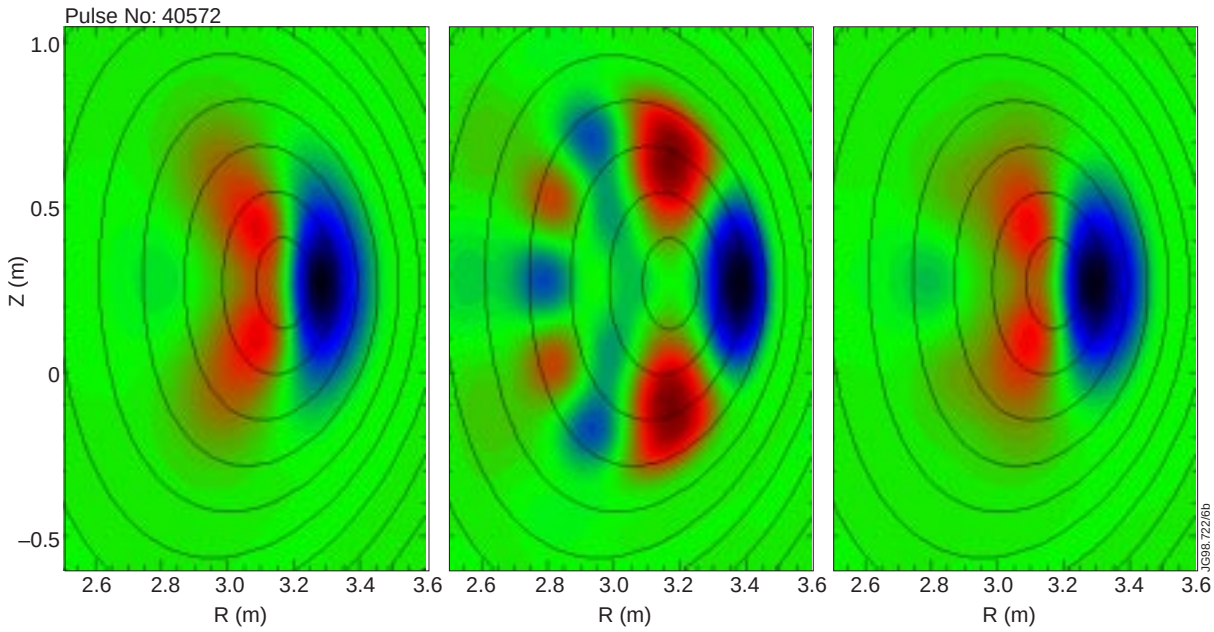

Fig.6b The perturbation of the SXR emission profile due to the disruption precursor. On the left is the n=1 component, in the middle the n=2 component and on the right the total perturbation. The lines are the equilibrium flux surfaces.

The equilibrium profile of the SXR emission is much more peaked and narrower than the electron temperature profile. (The SXR emission is proportional to $n_e n_i T_e^{\alpha}$ with $\alpha>1$, i.e. to the electron density, the ion density and the electron temperature all of which have peaked profiles.) The large gradients in the SXR equilibrium profile are within R=3.4m. This makes it more difficult to obtain a displacement from the perturbation of SXR emission by dividing by the gradient of the equilibrium profile, especially for R > 3.4 m. However, multiplying the displacement from the ECE with the gradient of the equilibrium SXR emission gives a prediction for the SXR perturbation. This prediction based on the ECE data is in reasonable agreement with the actual perturbation in the SXR emission.

2.2 Comparison of experimental and calculated mode structures

In this section the observed mode structures, which were analysed in detail in the previous section, are compared with mode structures calculated using the linearised ideal MHD model.

The theoretical mode structures are obtained by analysing the MHD stability of the equilibrium just before the disruption. The equilibrium profiles are taken from a transport analysis of

discharge #40572 with the TRANSP code [9]. The resulting pressure and q-profile at t=6.75s are shown in Fig. 7. The pressure profile is calculated from the ion temperature profile (from the charge exchange measurements), the electron temperature profile (from the ECE radiometer) and the electron density profile (from Thomson scattering). Included in the pressure profile is the contribution from the fast particles generated by the RF and neutral beam heating. The q-profile in TRANSP is calculated from the current diffusion equation which for this discharge results in a q-profile with low shear in the plasma centre and a minimum q of 1.75. In order to investigate the influence of different shapes of the central q-profiles (which is the least well known part of the equilibrium) a set of equilibria was calculated with the EFIT equilibrium reconstruction code [10]. In EFIT the equilibrium is reconstructed with a least squares fit to the measurements of 48 external magnetic pick-up coils and 14 flux loops. In this case the pressure profile from TRANSP is also included in the fit. The set of different equilibria was obtained by varying the prescribed value of q at the magnetic axis. The best fit in this series yields a q-profile which is very similar to the TRANSP q-profile.

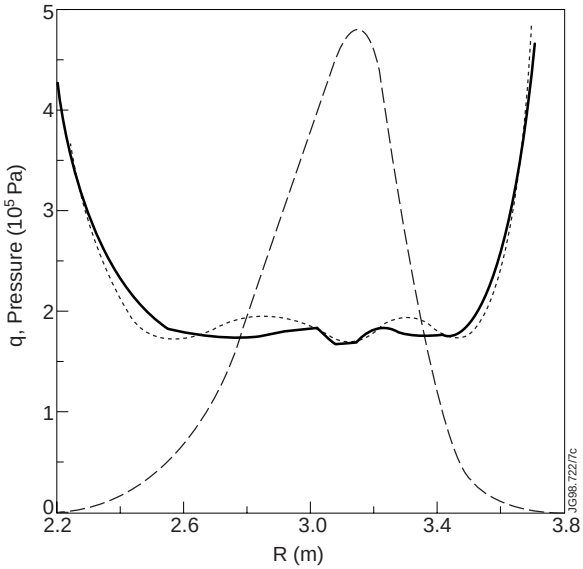

Fig.7 The profiles of the total pressure and the safety factor, q, as a function of the major radius for discharge 40572 at t=6.75s. Included is the q-profile from the EFIT reconstruction (dashed line).

The MHD stability of the equilibria is analysed with the Mishka-1 code [11]. The Mishka-1 code solves the linearised incompressible ideal MHD equation. However the stability boundaries in ideal MHD do not depend on the compressibility. The geometric quantities of the straight field line co-ordinate system used in the Mishka-1 code are calculated with the HELENA equilibrium code [12]. The co-ordinate system is the same as the co-ordinates used in the SXR tomography. The plasma boundary as determined by the EFIT equilibrium reconstruction is approximated by the 99% flux surface, i.e, just inside the separatrix of the single null plasma.

The equilibrium from the TRANSP analysis is calculated to be unstable (but close to the stability boundary, see next section) to a global pressure driven kink mode. The poloidal harmonics of the displacement perpendicular to equilibrium flux surfaces are plotted in Fig. 8 as a function of $\sqrt{\psi}$. The toroidal mode number is n=1. The mode extends over the whole plasma radius with the m=1 and m=2 as the dominant poloidal harmonics and the higher m as side bands. The poloidal harmonics are all in phase at the outboard, i.e. low field, side of the plasma. On the inboard side the m=1 and m=2 are out of phase and almost cancel each other out.

To compare the calculated mode structure with the structure obtained from the tomographic inversion of the SXR data, the displacement of the flux surfaces as shown in Fig. 8 has

to be multiplied by the gradient of the equilibrium SXR emission profile : $\delta(SXR) = \xi \bullet \nabla (SXR)$. The equilibrium SXR emission profile is obtained from the tomographic inversion of the time averaged SXR signals. It is assumed that the equilibrium SXR emission is a flux surface quantity, i.e. it can be described by a m=n=0 component. This is justified because the m=1 component when included in the inversion of the equilibrium emission has a negligible amplitude. This means that the peak of the SXR emission coincides with the magnetic axis. Due to the extreme peakedness of the equilibrium SXR emission profile, only the central part of the perturbation remains visible. Figure 9 compares the calculated perturbation of

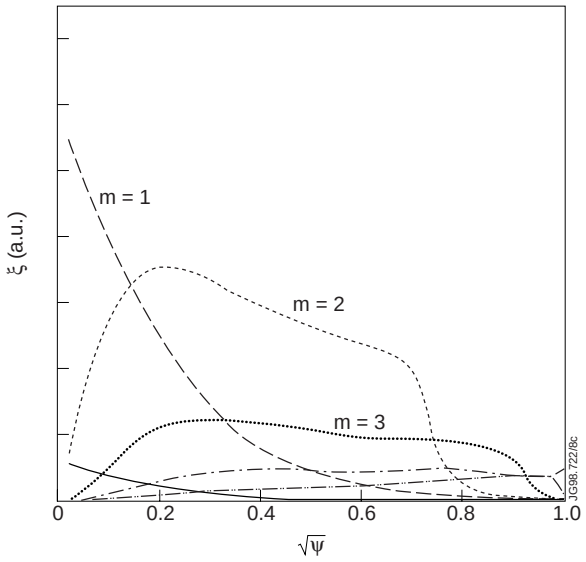

Fig.8 The poloidal harmonics of the perpendicular displacement as a function of the minor radius of the n=1 mode found unstable just before the disruption in discharge #40572.

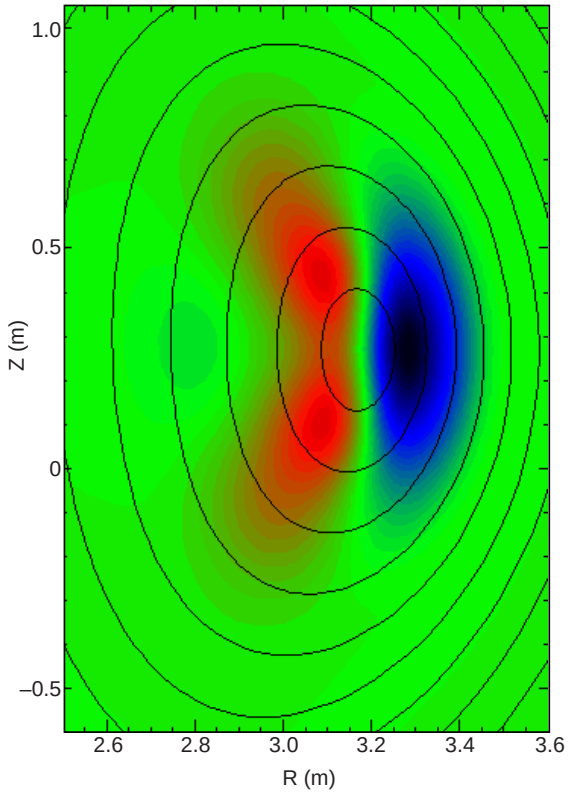

Fig.9a The n=1 perturbation of the SXR emission from the tomographic reconstruction.

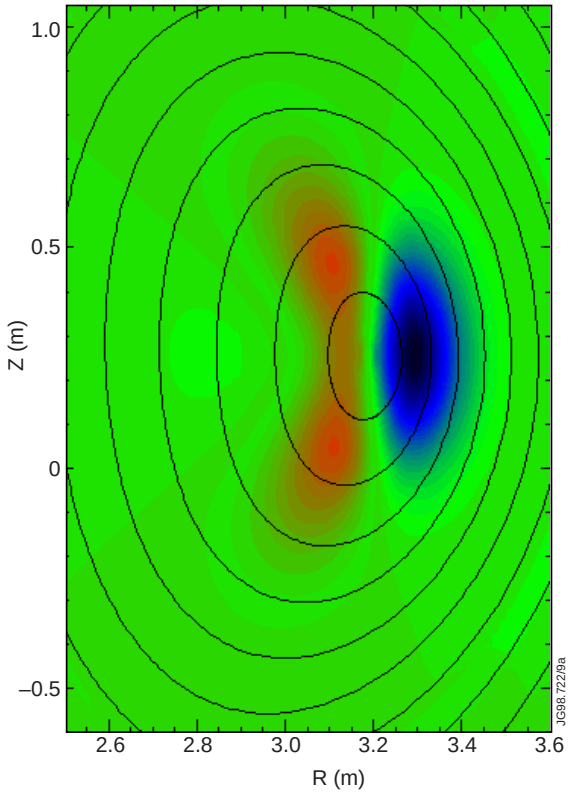

Fig.9b The simulated perturbation based on the theoretical mode structure from Fig. 8.

the SXR emission based on the mode structure of Fig. 8 with the perturbation resulting from the tomographic inversion. Good agreement between the experimental and theoretical perturbations is found. However due to the peaking of the SXR emission profile only information on the m=1

and m=2 harmonics can be obtained. The good agreement indicates that the disruption as observed in the Optimised Shear discharges is due to a global n=1 pressure driven kink mode exceeding the ideal MHD stability boundary. Similarly good agreement of the measured and calculated mode structures has been found in TFTR and DIII-D plasmas with internal transport barriers [14].

To investigate how much the mode structure of the pressure driven kink mode changes for different shapes of the central part of the q-profile, the mode structure is calculated for the family of equilibria obtained with the EFIT code with the central q varying between 1 and 2. If the mode structure is very sensitive to the value of q on axis or the minimum q then comparison with the tomography results can give an indication of the actual q-profile at the time before the disruption. Figure 10 shows the maximum amplitude of the different poloidal harmonics relative to the m=1 harmonic as a function of the minimum q value. The m=1 harmonic is always the largest component for q_{min} between 1 and 2. The ratio between the m=2 and the m=1, which can be determined from the SXR tomography, increases strongly with increasing q_{min} for q_{min} up to 1.5 . For larger q_{min} values the ratio is less sensitive to the value of q_{min}. Comparing these results with the experimental results gives a value for the minimum q between 1.5 and 2. The best agreement is for q_{min} ~ 1.7 with a q-profile (see Fig.7) which is very similar to the q-profile of the TRANSP equilibrium that was used for the comparison of Fig. 9. The error bars on the central part of the q-profile of about ±0.2 are such that it is not known whether the q-profile is monotonic or reversed in the plasma centre.

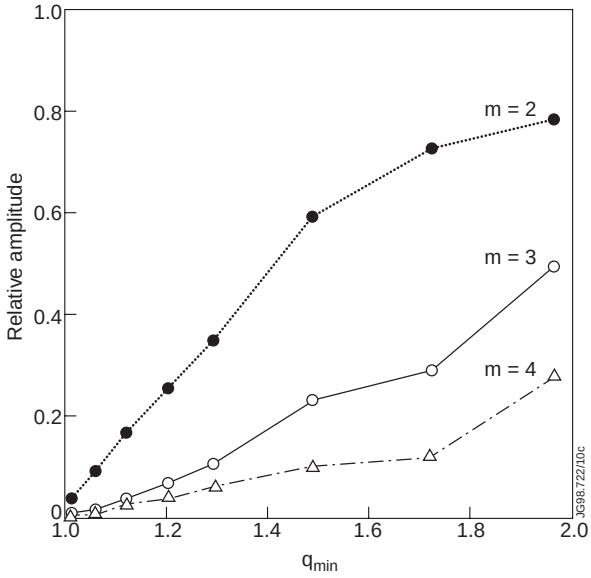

Fig.10 The maximum amplitude of the m=2, 3 and 4 poloidal harmonics of the pressure driven kink mode relative to the amplitude of the m=1 component as a function of the minimum q.

2.3 MHD Stability limits

In this section the stability limits due to the n=1 pressure driven kink mode, whose mode structure was shown to agree well with the observed disruption precursor, are analysed. The equilibria from the TRANSP analysis are used for the calculation of the stability limits for discharge #40572. For each time slice, the stability boundary is determined by raising or lowering the total pressure of the equilibrium while keeping the flux surface averaged toroidal current density profile and the shape of the pressure profile constant. In the calculations the plasma is surrounded by a vacuum and an ideally conducting wall. The position of the wall can have a significant influence on the stability of the global n=1 modes [13]. Here, the position and the shape of the ideally

conducting wall are the same as the JET vacuum vessel. The resulting evolution of the MHD stability in time are plotted in Fig. 11. Initially, at t=6.0 s the stability limit is extremely low at a normalised beta, β_N close to 1. At this time the β_N of the plasma is very close to the ideal MHD stability limit. Indeed, consistent with the calculated stability limits, it was found that in the experiment if the RF power is not stepped down at this point the plasma will disrupt. After t = 6.0 s , the stability limit slowly rises up to t = 6.6 s and the plasma is close to the stability limit during this time. This evolution is due to the changing shape of the pressure profile. With time the transport barrier in the JET Optimised Shear discharges moves outwards [2] following the evolution of the q=2 surface. This reduces the peaking factor of the pressure profile which considerably increases the MHD stability limit for the pressure driven kink mode.

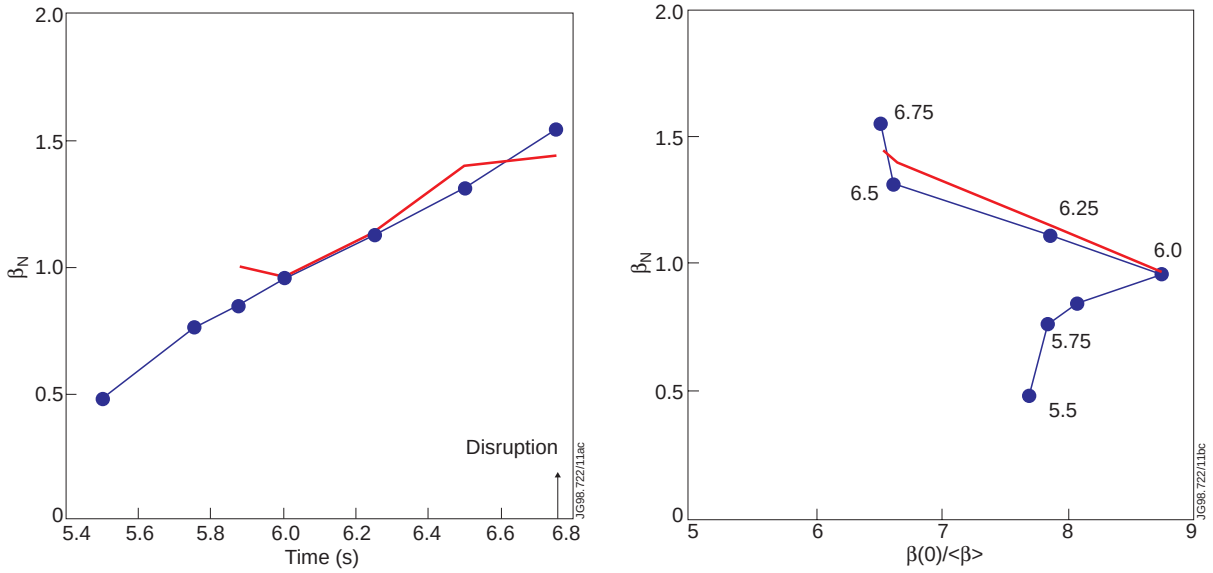

Fig.11 The evolution of the MHD stability limit for the n=1 pressure driven kink mode in discharge #40572 as a function of time (Fig 11a, on the left) and as a function of the peaking factor of the pressure profile (Fig. 11b, on the right). The curve without a symbol is the MHD stability limit for the n=1 kink mode. The lines with the filled circles are the experimental values.

This is also clear from Fig. 11b which shows the evolution of β_N of the stability limit and the experimental values as a function of the peaking factor of the pressure profile, (defined as $\beta(0) / <\beta>$ with $\beta(0)$ the beta value on the magnetic axis). At t = 6.6s the RF power is stepped up. Due to the central power deposition profile of the RF heating, the pressure profile peaking stays constant instead of decreasing further, while at the same time it increases the total pressure. As a consequence the plasma crosses the ideal MHD stability limit at which time a mode grows exponentially to large amplitude, leading to a disruption. Included in Fig. 2a are the time traces of a discharge (#40552) with very similar heating power up to t=6.6s. However in this discharge the RF power was not stepped up at t=6.6s and the disruption was avoided.

The influence of the central part of the q-profile on the MHD stability limit is shown in Fig. 12. The normalised beta at the stability limit is plotted as a function of the minimum q for the same set of EFIT equilibria with varying q on axis as was used in the previous section. The stability limit becomes much lower as the q on axis approaches q=1. However for q on axis

between 1.2 and 1.8 the stability limit is relatively insensitive to the details of the central q-profile. It varies about 10% between the local maximum at q=1.2 and the local minimum at q=1.7. The outer part of q-profile (q>2) does not change in this scan; also the total plasma current is fixed. The values in this plot are slightly higher than the value at t=6.75 in Fig. 11. This is due to a slightly lower peaking factor of the pressure profile and the lower central shear of the TRANSP equilibrium. As q_{min} approaches 2, a large part of the central q-profile is above 2 which leads to a significant increase in the marginally stable β_N .

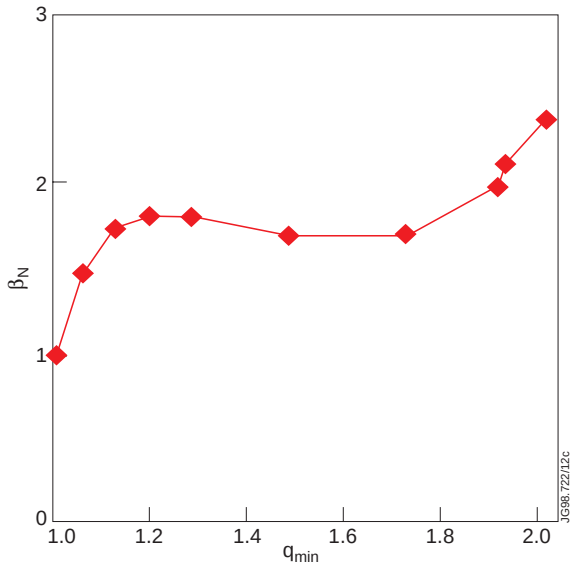

Fig.12 The n=1 MHD stability limit for different values of q_{min} keeping fixed the outer part of the q-profile, the total current and the pressure profile.

Another example of a disruption, in this case in a JET deuterium tritium DT discharge, is shown in Fig. 13. The Optimised Shear discharges in the DT campaign are described in detail in ref. [15]. In this discharge a total heating power of 23MW was applied in order to maximise the fusion power. This appears to be excessive: the transport barrier does not have the time to expand to larger radii and both the peaking factor of the pressure profile and β_N increase at the same time. This combination inevitably leads to a disruption. Figure 13b shows the evolution of the peaking factor and β_N and the stability boundary of the n=1 mode at the time just before the disruption. The q-profile from TRANSP is similar to that of #40572 with q on axis of 1.7.

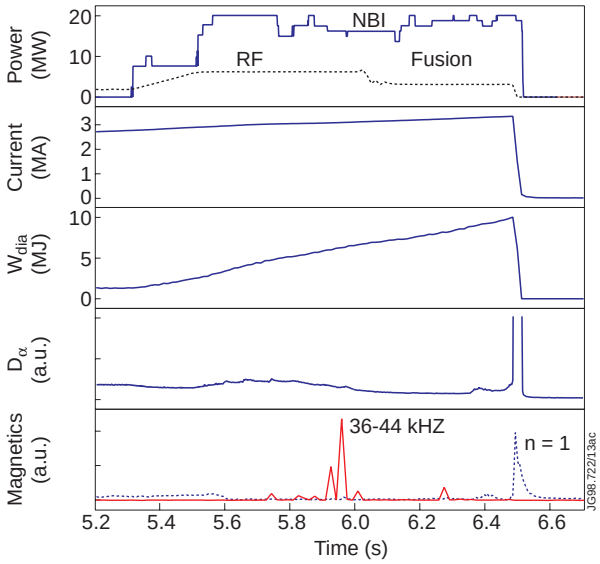

Fig.13a The traces for discharge #42940 of the NBI and RF heating power, the fusion power, the plasma current, the stored energy , and the magnetics signals for n=1 modes and a comb filter (36 to 44kHz)

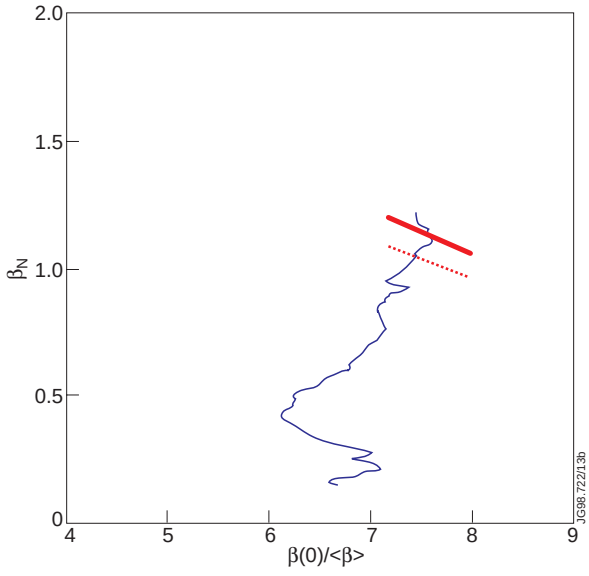

Fig.13b The MHD stability boundary for discharge #42940 and the experimental trace of β_N versus the pressure peaking factor. The thick red curve shows the stability boundary for the JET wall, the thin curve is the stability boundary without a conducting wall.

Finally in this section an example of a discharge without a disruption is analysed which achieved one of the highest neutron rates (5 10^{16} n/s) in deuterium OS plasmas (see Fig.14). This high performance has been achieved by operating the discharge very close to the MHD stability boundary (see Fig. 15) for more than 1 second. The operation close to the stability limit was made possible by real time control of the heating power [16]. The ICRH power is reduced at the time when the neutron rate (R_{nt}) reaches 2×10^{16} n/s. After this time, the neutral beam power is controlled to follow a prescribed R_{nt} waveform. Up to t=6.8s the plasma is in L-mode, i.e. there is no transport barrier at the plasma boundary. There is however a strong internal transport barrier. The peak neutron rate, $R_{nt} = 5.4\times10^{16}$ n/s, is obtained during this phase with a total heating power of 21 MW. The normalised beta is 1.8 at this time. After t=6.8s the plasma goes into H-mode which reduces the peaking factor of the pressure profile. During the H-mode phase the internal barrier slowly degrades and the discharge moves away from the stability limit. Most disruptions in the Optimised Shear discharges occur while the discharge is in L-mode. The added pressure at the boundary due to the edge pedestal reduces the peaking factor enough to avoid disruptions while

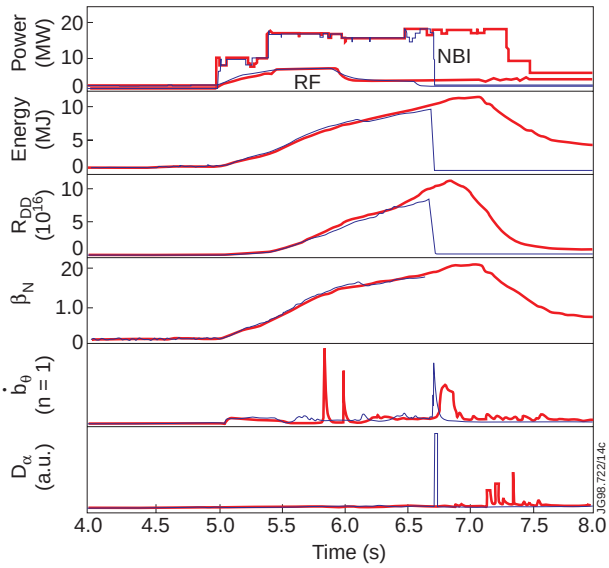

Fig.14 Time traces of the heating power, the reaction rate, the stored energy, normalised beta, the n=1 MHD signal and the D_α signal for two nearly identical discharges: 40847 (thick lines) and 40848 (thin lines) which ends in a disruption.

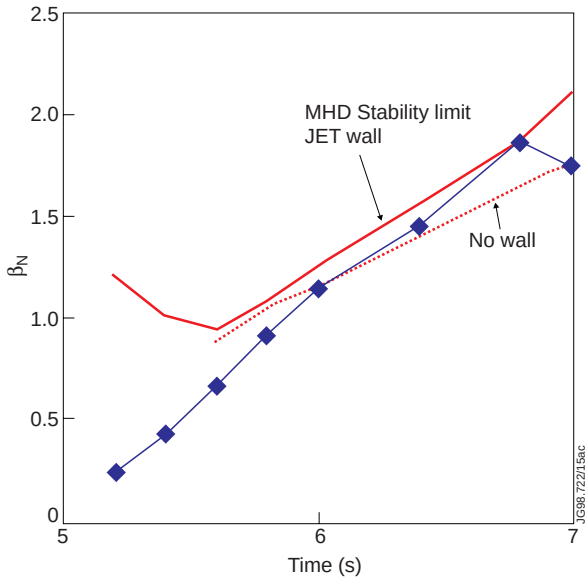

Fig.15a The stability limit with the JET wall and without an ideally conducting wall (broken line) as a function of time. Included is the evolution of the experimental normalised beta.

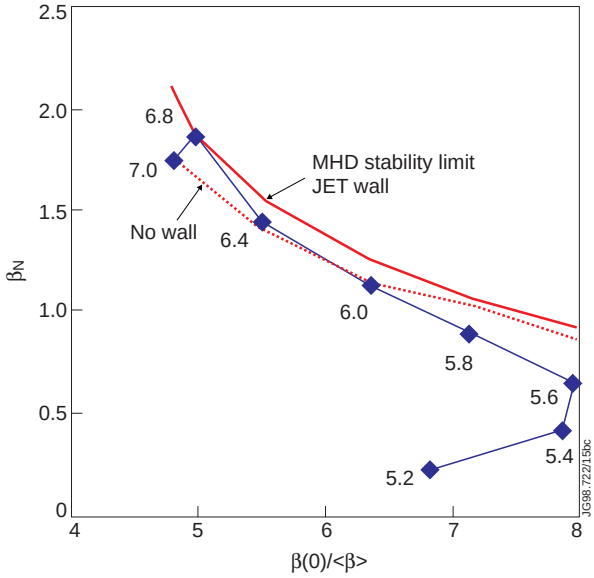

Fig.15b The evolution of the peaking factor of the pressure profile(from TRANSP data) and the normalised beta (β_N). Included is the MHD stability limit.

in H-mode. Included in Fig. 14 are the traces of a very similar discharge #40848, which, however, ends in a disruption illustrating how close the best JET high performance OS discharges are to a disruptive MHD stability limit.

Included in the stability diagram (Fig. 15b) is the stability limit due to the n=1 mode in the absence of an ideally conducting wall. For the extremely peaked pressure profiles early in the discharge the difference between the stability limits with the JET wall and without the wall is very small. For less peaked pressure profiles the no wall limit is significantly below the JET wall limit. The difference is due to the mode structures. At lower peaking factor the pressure gradient is more towards the boundary which increases the coupling of the dominant m=2 harmonic to the higher m harmonics which are more influenced by the stabilising influence of the wall. It appears that the discharge is above the calculated no-wall limit between t=6.2s and t=7.0s. Also in the DT discharge shown above the agreement between the occurrence of the disruption and the crossing of the stability limit is better with the JET wall limit than with the no-wall limit. In this case the no-wall limit is exceeded by 15% before the disruption occurs. However, with the pressure and q-profiles in the JET Optimised Shear discharges the difference between the no-wall and the JET wall stability limits is relatively small (<20%). The error bars in the stability limit due to error bars on the pressure peaking factor and especially the q-profile are too large to confirm that the JET vessel contributes to the wall stabilisation of the n=1 mode. Dedicated experiments, specifically with broad pressure profiles and q-profiles with q_{min} above 2 to maximise the difference between the JET wall and the no-wall stability limit, are needed to show the stabilising influence of the JET vessel.

3. FISHBONE-LIKE MODES

Instabilities with a fishbone like bursting behaviour occur in nearly all of the JET Optimised Shear discharges. Figure 16 shows the occurrence of these modes in JET DT discharge #42940 (see Fig. 13). During the burst the frequency of the mode rapidly changes from ~50-30 kHz down to ~30-15 kHz. The initial frequency is typically 20-30 kHz above the plasma rotation frequency. The toroidal mode number is predominantly n=1, however higher toroidal mode numbers n=2,3, .. are also commonly present in the same burst. In some cases the n=2 component is the dominant mode number.

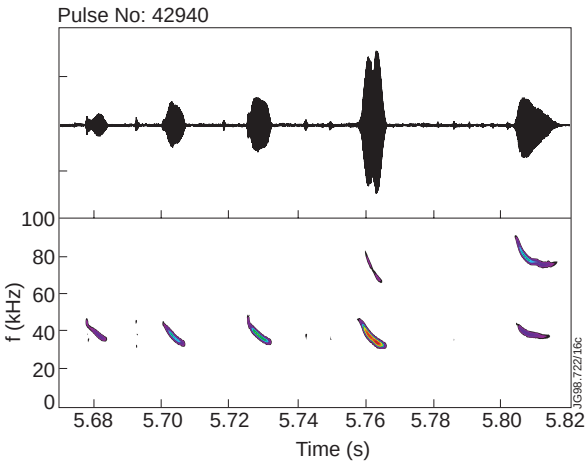

Fig.16 Example of a series of fishbone-like bursts in DT discharge #42940. The upper trace shows db_θ/dt from one magnetic pick-up coil. The lower trace gives a spectral analysis of this signal.

These instabilities are usually benign and do not cause any obvious harm to the plasma confinement or neutron rate. This was also found for the m/n=1/1 fishbone modes in the

conventional JET scenarios [22]. In a few discharges the mode grows to such a large amplitude, with a maximum displacement of up to 8 cm near the transport barrier, that it causes a temporary degradation of the confinement. The resulting heat pulse can cause a transition from L to H-mode which is usually unfavourable. After the transition to the H-mode edge the transport barrier at mid radius slowly degrades. An example of a large amplitude mode in the discharge with the highest DD neutron rate in JET #40554, is shown in Fig. 17. The mode causes a temporary drop of 10% in the neutron rate and a transition to the H-mode.

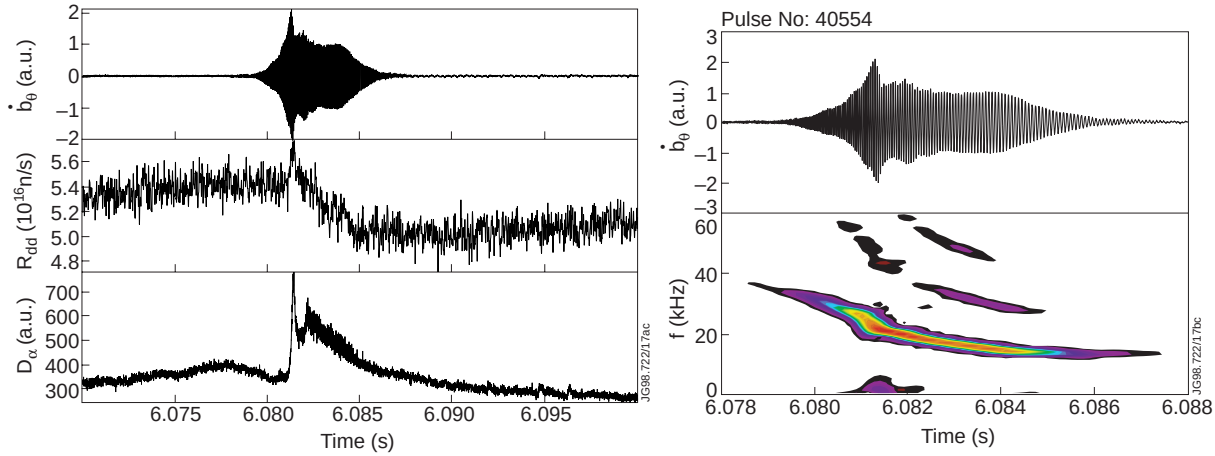

Fig.17 An example of a large amplitude fishbone-like mode which causes a temporary drop in the neutron rate and a transition to the H-mode. On the left are the time traces of one Mirnov coil, the D-D reaction rate and the D_α emission, on the right the expanded time trace of a Mirnov coil data and the evolution of the mode frequency.

The radial structure of the displacement of the modes can be inferred from SXR tomography and from ECE measurements, the results being in good agreement. Figure 18 shows the displacement, as calculated from the ECE data, for the large amplitude mode in #40554. The mode structure is almost identical to the mode structure of the disruption precursor in discharge #40572 (see Fig. 18) as discussed in section 2.

The conventional fishbone mode is thought to be a m/n=1/1 internal kink mode destabilised by the resonant interaction with fast particles through the precessional toroidal drift resonance [23]. Recently it was shown theoretically that the same resonance can also destabilise the so-called double kink modes [24] which are ideal pressure driven modes

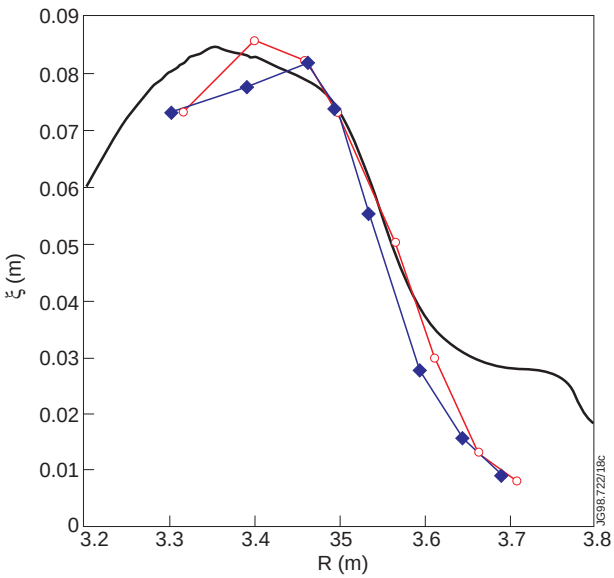

Fig.18 The displacement of the fishbone-like mode in discharge #40554 (see Fig.17) as a function of the major radius (filled diamonds). The magnetic axis is at R=3.2m, the plasma boundary at R=3.87m. Included in the figure (open circles) is the displacement due to the disruption precursor in #40572. The curve without symbols is the calculated ideal MHD displacement of the n=1 mode. The magnetic axis is at 3.2 m.

occurring for non-monotonic q-profiles. In particular, phenomena analogous to sawtooth stabilisation and fishbones excitation, related to the m/n=1/1 internal kink mode, are also expected for the double kink mode. Off-axis sawteeth have been observed in TFTR and Tore Supra in the region of the q=2 surface [25]. Sawtooth like modes extending up to the q=2 surface have been observed in some JET Optimised Shear discharges.

Without a contribution of fast particles the ideal MHD double kink mode becomes unstable when the minimum of a non-monotonic q-profile is just below an integer value [24]. For q_{min} just below 2 a double kink mode is localised inside the two q=2 surfaces and has a dominantly m=2 (n=1) poloidal (toroidal) mode number. The excitation of this mode by fast particles, when ideal MHD stable, is possible by resonance with the fast-ion precession drift frequency :

$$\omega_d \sim \frac{E}{ZeB_\theta R_0^2} \sim 2\pi E[MeV] \times 35kHz$$

where E is the fast-ion energy, Z the mass of the ions, B_θ the poloidal magnetic field and R_0 the major radius. The precessional drift frequency of the ICRH H-minority fast ions (E ~ 1MeV) is in reasonable agreement with the observed mode frequency in the plasma frame.

For an ICRH Maxwellian tail distribution, which is of relevance for the JET Optimised Shear discharges, the critical drop in fast particle beta across the width of the mode for destabilising the double kink mode is given by [26]:

$$\beta_h^{crit} \approx \frac{\omega_d}{\omega_A} \frac{\varepsilon}{0.15\Delta r / r_1} \frac{|s|\sqrt{1+2q^2}}{mq}$$

where s = r/q dq/dr is the magnetic shear at q=m/n (assumed to be the same magnitude for both surfaces), ε is the inverse aspect ratio, ω_d is the precessional drift frequency, ω_A the Alfven frequency, Δr and r_1 are the distance between the two rational surfaces and the average radius of the surfaces respectively. Thus, the low central shear in OS discharges can lead to a low critical β_h.

The JET Optimised shear discharges have a substantial fast particle content [6] driven by both the ICRH and the neutral beams. Just after the formation of the transport barrier when the plasma density is still low, the fast particle content is about 70 % of the total stored energy. The tail temperature of the fast ions at this time is of the order of 1 MeV. As the plasma density rises the fast particle fraction falls to 30% at the peak of the neutron rate and the tail temperature decreases to about 200 KeV.

The displacement due to the fishbone-like mode as measured by the ECE diagnostic (shown in Fig. 18) is a more global mode than the double kink mode used in Ref [24,26]. The difference is most likely due to absence of a second q = 2 surface in discharge #40554. The q-profile that gives the best agreement with the measured displacement and the calculated n=1 ideal MHD

displacement has a low central shear and a central q of 1.85. The experimental pressure profile used in the calculation of the mode structures is extremely peaked at the time of the mode, $p_0/\langle p \rangle = 7.5$.

The poloidal harmonics of the calculated displacement are shown in Fig.19. The mode structure is very similar to the mode structure calculated for the disruption precursor in discharge #40572 (see section 2). The total displacement along the horizontal axis at the height of the magnetic axis is included in Fig. 19. The agreement with the experimental displacement is very good in the central part of the plasma up to 3.6m (see Fig.18). However, the measured displacement does not show the finite amplitude due to the higher poloidal harmonics $m \geq 3$. The width of the displacement is determined by the position of the q=2 surface. The ratio of the amplitude in the plasma centre to the amplitude at the q=2 surface is governed by the value of q on axis (see Fig. 10).

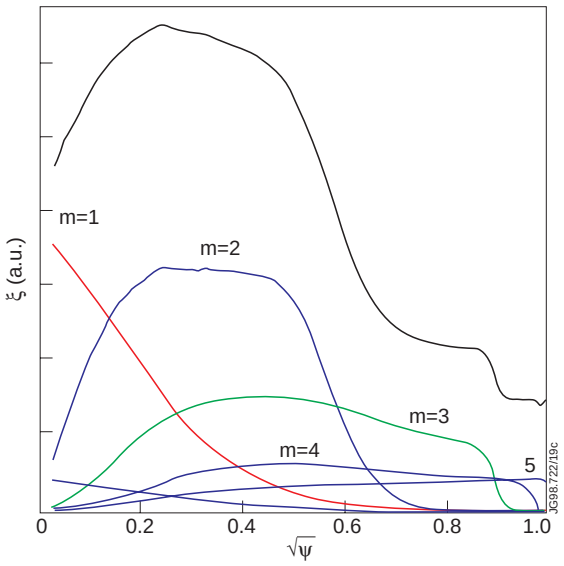

Fig.19 The poloidal harmonics of the calculated ideal MHD mode structure for discharge #40554 at t=16.08s as a function of the square root of the normalised poloidal flux. The upper curve is the sum of all harmonics, i.e. the total displacement in the outboard mid-plane.

Although the theory outlined above is for the double kink mode, equivalent fishbone modes should occur for any ideal MHD mode close to marginal stability. This has been examined with the CASTOR-K code [27] which numerically calculates the stability of a given mode structure in the presence of energetic ions. The CASTOR-K computes the additional drive due to the fast particles from the unperturbed particle orbits. The ideal MHD mode structure that matches the experimental displacement best (shown in Fig.19) is used in the analysis. The distribution of the ICRH ions used is a Maxwellian tail distribution with a tail temperature of 500keV: $f \sim (1-\psi)^4 \exp(-T / 500\ \text{keV})$. The computed drive due to the fast particles is shown in Fig. 20 as a function of the frequency of the oscillating ideal MHD mode. The results show that there is a relatively broad frequency band for which the fast particles are destabilising the mode. The frequency at the maximum in fast particle drive is a function of the tail temperature. For the tail temperature of 500 keV the optimum frequency is 16kHz. (For a 1MeV tail this frequency shifts to ~30 kHz.) These frequencies are in reasonable agreement with the observed frequencies for the fishbone like modes in JET, relative to the measured bulk plasma rotation.

Thus, it appears likely that the observed chirping modes belong to the same family as the disruptive modes (described in section 2) but are destabilised by a precessional drift resonance with trapped ICRH fast ions. This is supported by the fact that in some discharges the chirping mode changes continuously into the disruption precursor mode.

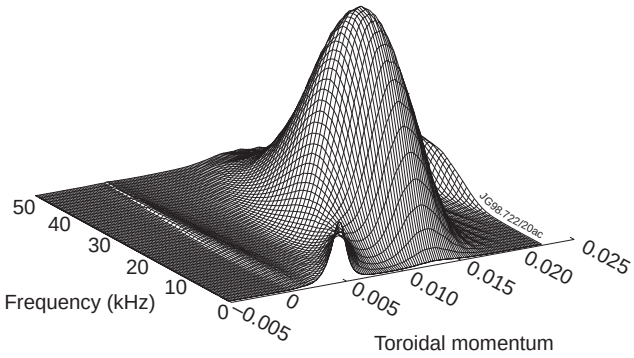

Fig.20a The radial (toroidal canonical momentum) contribution to the drive for a Maxwellian tail distribution with a temperature of 500 keV as a function of the mode frequency.

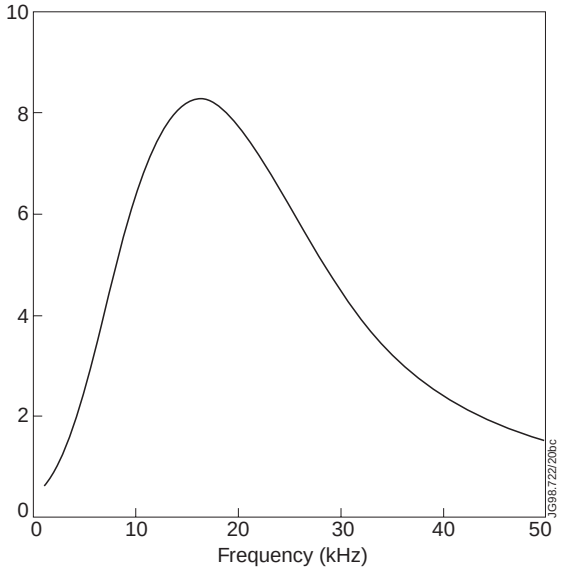

Fig.20b The total drive (radially integrated from Fig. 20a) due to the fast ions as a function of the mode frequency.

4. THE PICKET FENCE MODE

An unusual mode has been observed for the first time in the JET Optimised Shear discharges. It regularly appears at low frequency (200 - 700 Hz) during the L-mode phase, usually after the formation of the internal transport barrier. Its characteristic feature of a regular series of spikes in the D-alpha and magnetics time traces - reminiscent of a 'Picket Fence' - are shown in Fig. 21. The mode disappears abruptly at the L-H transition. It is localised close to the separatrix with only the one channel of the ECE diagnostic at 3.81m showing an abrupt change (i.e. fall in temperature) with each pulse. The mode as seen from a toroidal array of magnetic coils in Fig. 22 has a pulsed n=1 structure and is counter-rotating i.e. its motion is opposite to the bulk rotation of the plasma core driven by the neutral beams. The structure of the mode is localised along field lines (probably on the q=3 surface), similar to a snake oscillation [28].

As the mode occurs in the outer regions of the plasma where T_e is below 2keV, it is not seen directly in the SXR diodes. However both the ECE and the SXR data show regular oscillations in the plasma core when this mode is present. From SXR tomographic reconstruction these oscillations are interpreted as a bulk counter-clockwise motion of the plasma core generally at the same frequency as this mode with an amplitude of 4-6 mm. The mode may play a role in helping maintain the Optimised Shear discharges in L-mode and has occasionally appeared in high current neutral beam heated 'steady state' elmy H-mode discharges in JET, during periods when they have fallen into L-mode.

During operation with deuterium-tritium mixtures in the DTE1 Optimised Shear programme, this mode was far less prevalent - appearing only briefly in the early (deuterium rich) phase of a few OS discharges. Its general absence in these discharges may reflect the change in nature of the edge H-mode transport barrier with its formation at much lower power in D-T [15].

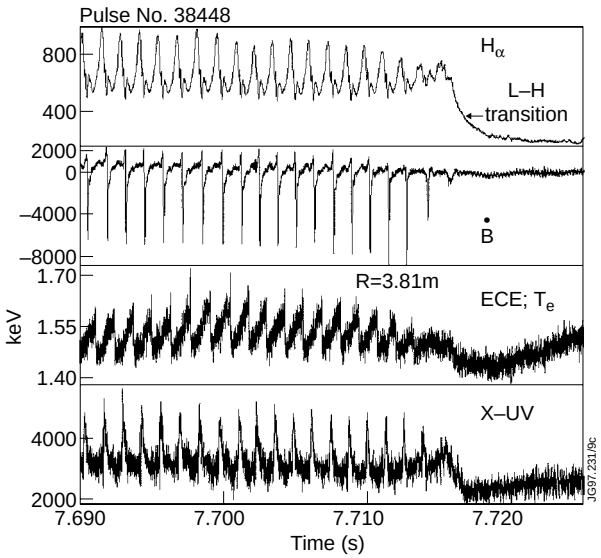

Fig.21 An example of the 'picket fence' mode seen in various edge diagnostics (D_α, magnetic pick-up coil, electron temperature (ECE) and X-UV radiation). It terminates with the onset of the H-mode (indicated in Figure).

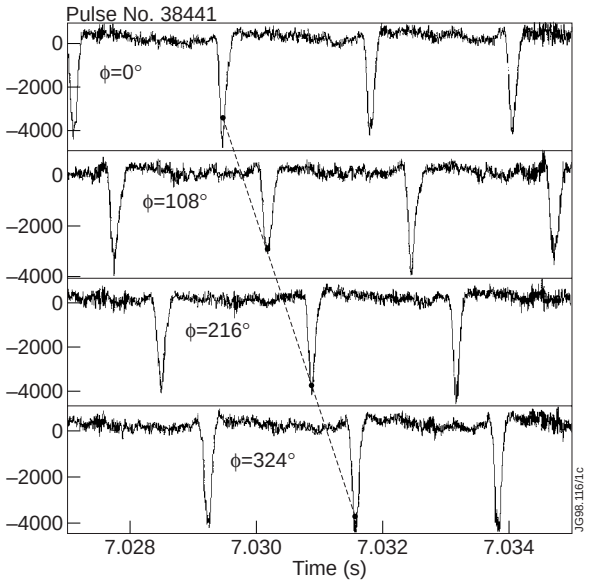

Fig.22 Signals from the toroidal array of magnetic pickup coils showing the counter rotating pulsed structure of the 'picket fence' mode.

5. SUMMARY AND CONCLUSIONS

During the high performance phase in the JET Optimised Shear discharges, the equilibrium profiles are characterised by a very peaked pressure profile and a q-profile with low shear in the plasma centre (with q on axis just below 2). The main limitation to the performance, i.e. neutron rate, is due to the occurrence of disruptions. The disruptions occur at relatively low values of the normalised beta, typically between 1 and 2. The mode structure just before the disruption was found to be a global mode without phase inversions, i.e an ideal MHD mode. The observed mode structures are in good agreement with the calculated mode structures for the n=1 ideal pressure driven kink mode. Also the experimental and calculated stability limits based on the linear MHD model are found to be in good agreement, confirming that the ideal pressure driven kink mode is responsible for the disruptions.

In the JET Optimised Shear discharges the transport barrier forms close to the plasma centre and moves radially outward during the evolution of the discharge. This leads to initially extremely peaked pressure profile, resulting in correspondingly low stability limits for the pressure driven kink mode. The best performing discharges are optimised to such an extent, using real time control of the heating power, that the discharge follows the calculated stability limit very closely for more than 1 second. During this time the stability limit increases by a factor 2 due to the changing shape of the pressure profile.

The chirping modes commonly observed in the JET optimised shear discharges have been found to have the same global mode structure as the mode responsible for the disruption precursor. In the case of the chirping modes, however, the modes are not driven by the thermal plasma

pressure as is the case for the disruptions but are instead driven by the fast particles created by the ICRH heating. Numerical calculations with the CASTOR-K code have confirmed that the global mode structures typical in the JET Optimised Shear discharges can be driven by resonant ICRH fast particles. This is in agreement with previous analytic results, based on the m/n=2/1 double kink mode, which showed that the influence of the fast particles on the stability of this mode is similar to that for the more conventional 1/1 internal kink where it can lead to fishbones. This leads us to the conclusion that the chirping modes observed in the JET Optimised Shear discharges can be interpreted as m/n=2/1 fishbone modes. As a consequence of the different driving mechanism the non-linear evolution of the modes is quite different. The chirping modes are benign except for the rare cases where they grow to a large amplitude. In those cases it leads to a small temporary drop of the neutron rate but more significantly it may trigger an H-mode after which the internal barrier degrades.

The good MHD understanding of these Optimised Shear discharges allows the examination of future scenarios. At present the q-profile and the pressure profile are not optimised and indeed not optimal with respect to the ideal MHD stability limit. The q-profiles have a low central shear with q on axis below 2. These q-profiles have been dictated by the requirement of the creation of a transport barrier at the available heating. This appears to require a q=2 surface with a small volume inside the q=2 surface. It is well known that this shape of the q-profile (see also Fig. 12) is not optimal with respect to the pressure driven kink stability limit.

The very high values for normalised beta calculated to be MHD stable, $\beta_N \sim 5$ (in the presence of stabilisation due to an ideally conducting wall), reported in [17-19] require a q-profile with the minimum q above 2 and a broad pressure profile. Without wall stabilisation the beta limit is much reduced for the q-profile with $q_{min} > 2$. A better choice in that case is to maximise the normalised current, $I_N = I/(a\,B)$ This leads to a q-profile with q_{min} close to but above 1 [20]. In the case of a JET-like plasma shape it was shown in Ref. [20] that the beta limit can still be as high as 3.7 without wall stabilisation. However here also it requires a broad pressure profile ($p_0/\langle p\rangle \sim 2.5$-3). It is not clear whether a broad pressure profile is consistent with the presence of a transport barrier and the corresponding large local pressure gradients. The present JET q-profiles appear to be in between the two envisaged optimal operating points, however, with a pressure peaking factor which is almost a factor of two larger than the optimum value found in [17-20]. Optimising both the shape of the q-profile and the pressure profile may lead to substantially better performance in the JET Optimised Shear plasmas.

ACKNOWLEDGEMENT

The UKAEA authors were jointly funded by the UK Department of Trade and Industry and EURATOM.

APPENDIX SXR TOMOGRAPHY USING A STRAIGHT FIELD LINE CO-ORDINATE SYSTEM

The method for the tomographic reconstruction of the SXR emission uses a co-ordinate system based on the equilibrium flux surfaces. The poloidal angle is such that the magnetic field lines appear straight. This choice of poloidal angle has a larger separation of the lines of constant angle on the low field side which leads to a natural representation of mode structures which are more extended in poloidal angle on the low field side (the so-called θ^* effect). This co-ordinate system is the same straight field line flux co-ordinate system that is used in the MHD stability calculations [11]. The magnetic axis of the equilibrium used as a co-ordinate system is adjusted such that the maximum of the equilibrium SXR emission profile is in the same position as the magnetic axis. This reduces the number of poloidal harmonics needed to represent the mode structures of the perturbations.

The perturbation of the SXR emission are represented with a set of basis functions :

$$S(\psi,\theta) = \sum_{i,m} a_{i,m} H(s-s_i) \cos(m\theta+n\phi) + b_{i,m} H(s-s_i) \sin(m\theta+n\phi) \qquad (A.1)$$

where S is the SXR perturbation, s is $\sqrt{\psi}$ with ψ the normalised poloidal flux, θ (ϕ) the poloidal (toroidal) angle, m (n) the poloidal (toroidal) harmonic and H is basis function for the radial (ψ) dependence. H is chosen as a radially localised B-spline. The expansion coefficients $a_{i,m}$ and $b_{i,m}$ are the unknowns to be determined from the SXR data.

For every basis function the line integral along each of the viewing lines of the SXR cameras is calculated. This gives a matrix with the relative contribution of each basis functions to each of the viewing lines. Multiplying the matrix with the vector of (unknown) expansion coefficients will give the measurement for each viewing line. The resulting system of equations $\mathbf{M}(n_v \times n_c)\ \mathbf{c}(n_c) = \mathbf{x}(n_v)$ for the unknowns $a_{i,m}$ and $b_{i,m}$ is over-determined if the number of viewing lines (n_v) is larger then the number of expansion coefficients (n_c).

The system of equations is solved using singular value decomposition (SVD). This amounts to a least-squares fit of the expansion coefficients to the measurements. Weights can be given to each of the measurements. The results can be filtered (smoothed) by limiting the total number of singular values, i.e excluding small values. The distribution of singular values also gives an indication whether the number of expansion coefficients is too large.

In cases where the perturbation to be reconstructed is growing slowly compared to the rotation frequency, the measurements at different times can be interpreted as coming from different toroidal angles (assuming a rigid toroidal rotation of the mode structure). This enlarges the number of independent measurements without increasing the number of expansion coefficients. Alternatively, it allows to use more than one toroidal mode number in the tomographic reconstruction.

REFERENCES

[1] GORMEZANO C., and the JET team, Plasma Phys. and Contr. Nucl. Fusion Research 1997 (Proc. 16th Int. Conf., Montreal, 1996), Vol. I IAEA, Vienna (1997) 487.

[2] SOLDNER F.X. et al., submitted to Nucl Fusion (1998).

[3] NAVE M.F.F. et al., Nuclear Fusion **37** (1997) 809.

[4] HUYSMANS G.T.A. et al., Nuclear Fus **38** (1998) 179.

[5] SHARAPOV S.E. et al., submitted for publication in Nucl Fusion (1998).

[6] BARANOV Y. et al., submitted for publication in Nucl Fusion (1998).

[7] BARTLETT D.V. et al., Proc.9th Int. Workshop on ECE and ECRH, Borrego Springs, USA (1995), EC-9, 511 (World Scientific, Singapore).

[8] ALPER B., et al, Rev. Sci. Instr. **68**, (1997) 778.

[9] GOLDSTON R.J., et al., J. Comput. Phys. **43** (1981) 61.

[10] LAO L. et al. , Nucl. Fusion **30** (1990) 1035.

[11] MIKHAILOVSKII A.B., HUYSMANS G.T.A., KERNER W.O.K., SHARAPOV S.E., Plasma Phys. Rep., **23** (1997) 844.

[12] HUYSMANS G.T.A., GOEDBLOED J.P., and KERNER W.O.K., CP90 Conf. on Comp. Physics Proc., World Scientific Publ. Co. (Ed. A. Tenner), 1991, p.371

[13] TURNBULL A.D., TAYLOR T.S., CHU M.S., MILLER R.L., LIN LIU Y.R., Nuclear Fusion **38** (1998) 1467.

[14] STRAIT E.J., et al., Phys Plasmas **4** (1997) 1783.
DIII-D Team, Plasma Phys. and Contr. Nucl. Fusion Research 1997 (Proc. 16th Int. Conf., Montreal, 1996), Vol. I IAEA, Vienna (1997) 95.
MANICKAM J., et al., Plasma Phys. and Contr. Nucl. Fusion Research 1997 (Proc. 16th Int. Conf., Montreal, 1996), Vol. I IAEA, Vienna (1997) 453.
HENDER T.C., et al., 23rd EPS Conf. Contr. Fusion and Plasma Physics, Kiev 1996, Vol. 20C, p31.

[15] GORMEZANO C. et al., Phys. Rev Lett. **80** (1998) 5544.

[16] SIPS A.C.C. et. al., Plasma Phys. Control. Fusion **40** (1998) 1171.

[17] KESSEL C., et al., Phys Rev. Lett. **72** (1994) 1212.

[18] TURNBULL A.D. et al., Phys Rev. Lett. **74** (1995) 718.

[19] LEE B.J., TURNBULL A.D., and TAYLOR T.S., Nucl Fusion **37** (1997) 1271.

[20] BONDESON A. et al., Nucl Fusion, **37** (1997) 1419.

[21] NAVE M.F.F. et al., Nucl. Fusion **31** (1991) 697.

[22] CHEN L. et al., Phys. Rev. Lett. **52** (1984) 1122.

COPPI B. et al., Phys. Rev. Lett. **63** (1989) 2733.

[23] HELANDER P. et al., Phys. Plasmas **4** (1997) 2181.

[24] GIMBLETT C.G. et al., Phys. Plasmas **3** (1996) 3369.

[25] TURLUR S. et al., Proceedings EPS Conf. Controlled Fusion and Plasma Physics, Berchestgaden 1997, Vol IV, p73; Z. Chang et al., Phys Rev. Lett. **77** (1996) 3553.
[26] HENDER T. et al., Proceedings of the Varenna Theory Workshop (1998), P. Helander et al., Proceedings EPS Conf. Controlled Fusion and Plasma Physics (1998).to be published.
[27] D.N. Borba, Ph.D. Thesis, Universidade Tecnica de Lisboa (1997).
[28] GILL R.D., et al., Nucl. Fusion **32** (1992) 723.